

1 Response of water vapour D-excess to land-
2 atmosphere interactions in a semi-arid
3 environment

4
5 Stephen D. Parkes¹, Matthew F. McCabe^{1,2}, Alan D. Griffiths³, Lixin Wang⁴, Scott Chambers³,
6 Ali Ershadi^{1,2}, Alastair G. Williams³, Josiah Strauss², Adrian Element³

7
8 ¹ Water Desalination and Reuse Centre, King Abdullah University of Science and Technology
9 (KAUST), Jeddah, Saudi Arabia

10 ² Department of Civil and Environmental Engineering, University of New South Wales, Sydney,
11 Australia

12 ³ Australian Nuclear Science and Technology Organization, Sydney, New South Wales,
13 Australia

14 ⁴ Department of Earth Sciences, Indiana University–Purdue University Indianapolis (IUPUI),
15 Indianapolis

16

17 Corresponding Author: Stephen Parkes, stephen.parkes@kaust.edu.sa

18 Keywords: Stable isotopes, D-excess, water vapour, land-atmosphere coupling

19

20 Key points:

- 21 • Examine the influence of local land-atmosphere coupling on water vapour isotopes
- 22 • Diurnal cycle of D-excess in water vapour is determined by an interplay between large
23 scale moisture sources and nocturnal processes
- 24 • The D-excess of the evaporation fluxes impose negative forcing on the ambient vapour
- 25 • Nocturnal D-excess values are determined by surface exchange and turbulent mixing

26 **Abstract**

27 The stable isotopic composition of water vapour provides information about moisture sources and
28 processes difficult to obtain with traditional measurement techniques. Recently, it has been
29 proposed that the D-excess ($d_v = \delta^2\text{H} - 8 \times \delta^{18}\text{O}$) of water vapour can provide a diagnostic tracer
30 of continental moisture recycling. However, D-excess exhibits a diurnal cycle that has been
31 observed across a variety of ecosystems and may be influenced by a range of processes beyond
32 regional scale moisture recycling, including local evaporation (ET) fluxes. There is a lack of
33 measurements of D-excess in evaporation (ET) fluxes, which has made it difficult to assess how
34 ET fluxes modify the D-excess in water vapour (d_v). With this in mind, we employed a chamber
35 based approach to directly measure D-excess in ET (d_{ET}) fluxes. We show that ET fluxes imposed
36 a negative forcing on the ambient vapour and could not explain the higher daytime d_v values. The
37 low d_{ET} observed here was sourced from a soil water pool that had undergone an extended drying
38 period, leading to low D-excess in the soil moisture pool. A strong correlation between daytime d_v
39 and locally measured relative humidity was consistent with an oceanic moisture source, suggesting
40 that remote hydrological processes were the major contributor to daytime d_v variability. During
41 the early evening, ET fluxes into a shallow nocturnal inversion layer caused a lowering of d_v values

42 near the surface. In addition, transient mixing of vapour with a higher D-excess from above the
43 nocturnal inversion modified these values, causing large within night variability. These results
44 indicate d_{ET} can generally be expected to show large spatial and temporal variability and to depend
45 on the soil moisture state. For long periods between rain events, common in semi-arid
46 environments, ET would be expected to impose negative forcing on the surface d_v . Spatial and
47 temporal variability of D-excess in ET fluxes therefore needs to be considered when using d_v to
48 study moisture recycling and during extended dry periods with weak moisture recycling may act
49 as a tracer of the relative humidity at the oceanic moisture source.

50

51 **1 Introduction**

52 Climate change has the potential to significantly impact surface and atmospheric water budgets.
53 Our best understanding of future exchanges between the atmospheric water cycle and the land
54 surface on a regional to global scale, is likely to be gained through analysis of numerical
55 simulations (Decker et al. 2015; Evans and McCabe, 2010; Harding and Snyder, 2012; Wei et al.
56 2012). Consequently, continual improvement of available models is essential, but is contingent
57 upon ongoing validation and evaluation of model performance over a broad range of landscapes
58 and climate types (McCabe et al., 2016). To do this effectively, a diversity of datasets that directly
59 quantify processes represented within these models are required (McCabe et al., 2005).
60 Unfortunately, datasets that directly measure land-atmosphere exchange at the process level are
61 limited (Jana et al., 2016).

62 Water is composed of a number of stable isotopologues that have sufficient abundance to be
63 measured in atmospheric water vapour ($^1\text{H}_2^{16}\text{O}$, $^1\text{H}^2\text{H}^{16}\text{O}$, $^1\text{H}_2^{18}\text{O}$ and $^1\text{H}_2^{17}\text{O}$). The deviation of
64 the isotope ratios, reported as

$$65 \quad \delta = \left[\frac{R_{\text{sample}}}{R_{\text{VSMOW}}} - 1 \right] \text{‰} \quad (1)$$

66 where R is the isotope ratio ($^2\text{H}/^1\text{H}$ or $^{18}\text{O}/^{16}\text{O}$) and VSMOW (Vienna Standard Mean
67 Ocean Water), is the international standard for reporting water isotope ratios, and have potential
68 to evaluate land-atmosphere exchange by discriminating processes based on their isotopic
69 signature (Berkelhammer et al. 2013; Lee et al. 2009; Noone et al. 2013; Risi et al. 2013). Isotopic
70 ratios of water vapour ($\delta^2\text{H}$ and $\delta^{18}\text{O}$) can therefore provide information that is complimentary or
71 even unobtainable when using conventional measurement techniques.

72 The utility of water isotope ratios for tracing sources of moisture derives from the characteristic
73 equilibrium and kinetic isotopic fractionation that occurs when water undergoes a phase change,
74 causing light water molecules to preferentially accumulate in the vapour phase. Soil moisture is
75 typically enriched in heavy isotopes relative to the ocean (Gat, 1996), so water vapour derived
76 from land surface evaporation is expected to have a different isotopic composition to moisture
77 evaporated from the ocean. This has led to a number of studies using stable isotopes in precipitation
78 to partition oceanic and land derived sources (Froehlich et al. 2008; Tian et al. 2001). However,
79 land-atmosphere exchange is not restricted to periods of precipitation, and there are relatively few
80 studies examining the role of land-atmosphere exchange on ambient humidity budgets using stable
81 isotope observations of vapour (e.g. Aemisegger et al. 2014; Risi et al. 2013).

82 In addition to the source of moisture, the magnitude of isotopic fractionation that occurs when
83 water evaporates is related to the liquid surface temperature and humidity gradient between the
84 evaporating surface and atmosphere (Craig and Gordon, 1965). The temperature dependent
85 equilibrium exchange between liquid and vapour is the largest contributor to isotopic fractionation
86 during evaporation, with the fractionation for ^2H approximately a factor of 8 greater than ^{18}O .
87 The effect of kinetic fractionation associated with moisture diffusing from the thin laminar layer
88 of vapour in equilibrium with the water surface to the turbulent atmosphere above is influenced by
89 the relative humidity of the atmosphere and wind speed (Merlivat and Jouzel, 1979). The kinetic
90 fractionation factors for ^2H and ^{18}O are similar, causing the ratio of ^2H to ^{18}O in the
91 evaporating vapour to decrease as kinetic effects increase with decreasing relative humidity. This
92 phenomenon has been observed for evaporative conditions over the Mediterranean sea (Gat et al.
93 2003; Pfahl and Wernli, 2009) and the Great Lakes in Northern USA (Gat et al. 1994; Vallet-
94 Coulomb et al. 2008).

95 The D-excess parameter ($\text{D-excess} = ^2\text{H} - 8 \times ^{18}\text{O}$) (Dansgaard, 1964), quantifies the non-
96 equilibrium isotopic fractionation. A reproducible relationship between the D-excess and relative
97 humidity near the ocean surface has been observed across a wide range of locations (Kurita, 2011;
98 Pfahl and Wernli, 2008; Steen-Larsen et al. 2015; Uemura et al. 2008). Therefore, it has been
99 suggested that for precipitation, D-excess is a good tracer of sea surface evaporative conditions
100 (Masson-Delmotte et al. 2005; Merlivat and Jouzel, 1979). However, this view has recently been
101 challenged due to the role local and regional scale land-atmosphere coupling has in modifying the
102 D-excess of atmospheric humidity over diurnal (Lai and Ehleringer, 2011; Simonin et al. 2014;
103 Welp et al. 2012; Zhao et al. 2014) and synoptic timescales (Aemisegger et al. 2014). As evidence

104 for the role ET plays in modifying the D-excess of water vapour (d_v), a diurnal cycle of d_v near the
105 land surface across a range of land surface types has been observed (Berkelhammer et al. 2013;
106 Simonin et al. 2014; Welp et al. 2012). The diurnal cycle shows higher values in the day, which
107 has been proposed to be driven by entrainment (Lai and Ehleringer, 2011; Welp et al. 2012), local
108 evapotranspiration sources (Simonin et al. 2014; Zhao et al. 2014) and meteorological conditions
109 affecting the D-excess of the evaporative fluxes (d_{ET}) (Welp et al. 2012; Zhao et al. 2014), coupled
110 with low nocturnal values resulting from equilibrium exchange between liquid and vapour pools
111 (Simonin et al. 2014) and dew fall (Berkelhammer et al. 2013). For synoptic scales, Aemisegger
112 *et al.* (2014) showed that moisture recycling from the land surface had a significant impact on d_v
113 for *in-situ* measurements in Switzerland. These studies have largely relied on isotopic models to
114 assess the contribution of ET fluxes, but a lack of d_{ET} measurements make it difficult to draw
115 robust conclusions.

116 The evidence provided by these studies suggest d_v is a tracer of moisture recycling both on diurnal
117 and synoptic time scales, and is influenced by dynamics of surface moisture budgets in the
118 atmospheric boundary layer (ABL). However, as noted by Welp *et al.* (2012), ET and entrainment
119 fluxes both increase as the ABL grows through the previous days residual layer, which can make
120 interpreting the role of local moisture recycling on d_v difficult. To overcome this, Simonin *et al.*
121 (2014) used a trajectory model to simulate the D-excess of vapour evaporated over the ocean. As
122 the d_v was greater than the modelled oceanic moisture source, it was assumed that high daytime
123 values were supported by local ET fluxes. Zhao *et al.* (2014) suggested that since, on cloudy days,
124 no diurnal cycle was observed for the d_v , that ET fluxes played a dominant role. Whilst these
125 studies provide compelling evidence for the role of ET driving the diurnal cycle of d_v , no

126 measurements of d_{ET} were made. To date the only measurements of d_{ET} have been presented by
127 Huang *et al.* (2014) over a maize crop in north west China. Interestingly, their direct measurements
128 conflicted with previous interpretations and showed that the d_{ET} invoked a negative forcing on d_v ,
129 even though a strong diurnal cycle of high values in the day and low values at night were observed.
130 In order to better interpret the role of local moisture recycling on the diurnal cycle of d_v ,
131 measurements of d_{ET} are required to assess if the negative forcing is consistent in different
132 ecosystems.

133 The aim of this work is to provide much needed d_{ET} measurements to investigate how ET fluxes
134 modulate the d_v diurnal cycle. To do this, chamber based measurements of the ET flux isotopic
135 compositions were combined with *in-situ* measurements of water vapour isotope ratios,
136 meteorological and radon concentration observations. The data was collected in a region of the
137 semi-arid Murray Darling basin in south-eastern Australia. These data represent the first such
138 collection of the ^2H , ^{18}O and D-excess in water vapour from this region of Australia. The
139 augmentation of the chamber based measurements with *in-situ* observations provide a framework
140 to directly assess the role local ET fluxes have on ambient vapour D-excess.

141 **2 Methods**

142 **2.1 Site Description**

143 During the austral autumn of 2011, a field campaign covering the period April 27 to May 11 was
144 conducted at the Baldry Hydrological Observatory (BHO) (-32.87, 148.54, 460 m above sea level)
145 located in the central-west of New South Wales, Australia (Figure 1). The climate of the region is
146 characterised as semi-arid with no clear wet season, a mean annual rainfall of 600 mm, and a mean
147 annual temperature of 24.2°C (source Australian Bureau of Meteorology, 2015,

148 <http://www.bom.gov.au/>). The BHO grassland eddy covariance flux tower was the central site of
149 measurements and was located in a natural grassland paddock of dimensions approximately 900m
150 (north-south) by 300m (west-east), with a gentle slope decreasing in elevation by approximately
151 20 m from southeast to northwest. The flux tower was located 650 m from the road to the south
152 and 200 m from a reforested paddock to the west. The forest site to the west and southwest was
153 reforested in 2001 with *Eucalyptus camaldulensis*, *Eucalyptus crebra* and *Corymbia maculate*. At
154 the time of the campaign these trees were approximately 10 m tall. All other adjacent paddocks
155 and most of the surrounding region had similar surface characteristics to the grassland
156 measurement site.

157 **2.2 Water stable isotope analyses**

158 **2.2.1 *In-situ* water vapour calibration and sampling**

159 In-situ water vapour isotope ratios were monitored using a Wavelength Scanning Cavity Ring
160 Down Spectrometer (WS-CRDS L115-I, Picarro Inc., Sunnyvale, CA, USA), while flux chambers
161 were interfaced to an Off Axis Integrated Cavity Output Spectrometer (OA-ICOS, DLT100, Los
162 Gatos Research (LGR), Mountain View, CA, USA) to determine the isotopic composition of ET
163 fluxes. Using an automated continuous flow calibration system (built in-house), we simultaneously
164 determined calibration coefficients for both analysers. Calibration experiments were designed to
165 determine the water vapour mixing ratio cross-sensitivity of isotope ratios and linearity of the $\delta^2\text{H}$
166 and ^{18}O measurements. More details on the calibration procedure are found in the supplementary
167 materials. Due to logistical constraints, the calibration system was not transported into the field,
168 so corrections were determined by compositing multiple calibration experiments run before and
169 after the campaign.

170 During the campaign, a secondary portable calibration system was employed to monitor time
171 dependent drift of the Picarro analyser (CTC HTC-Pal liquid autosampler; LEAP Technologies,
172 Carrboro, NC, USA). Two standards spanning expected water vapour ^2H (-49.1 and -221.9‰)
173 and ^{18}O (-9.17 and -27.57‰) ranges were injected at approximately 18 mmol.mol⁻¹ on three
174 occasions during the campaign.

175 The uncertainty of measurements from both isotopic analysers was estimated by applying mixing
176 ratio cross-sensitivity and linearity corrections to all calibration measurements collected prior,
177 during and after the campaign. For the Picarro instrument, measurement uncertainty was 0.8, 0.2
178 and 1.9‰ for $\delta^2\text{H}_v$, $\delta^{18}\text{O}_v$ and d_v , respectively. No calibrations were performed for the LGR in
179 field, so the measurement uncertainty was estimated by compositing calibration measurements
180 made before and after the campaign, which were 0.9, 0.4 and 3.3‰ for ^2H , ^{18}O and d_v .

181 Although no calibration experiments were run on the LGR during the campaign, simultaneous *in-*
182 *situ* measurements were made with the Picarro when chamber measurements were not operated.
183 During the day, average differences were -0.06 (± 2.0), 0.13 (± 0.5) and 0.4 (± 3.3)‰ for ^2H , ^{18}O
184 and d_v , respectively. A comparison of the analysers is shown in figure S1. At night, while the
185 Picarro was able to maintain a steady cavity and optical housing temperature, the LGR cavity
186 temperature dropped by up to 8°C. In response to the drop in cavity temperature, night time LGR
187 measurements of $\delta^{18}\text{O}$ and d_v and to a lesser extent the $\delta^2\text{H}$, were physically unrealistic and
188 discarded from subsequent analyses. Chamber measurements were therefore restricted to between
189 09:00 (when the LGR cavity temperature had stabilised and *in-situ* measurements were again in
190 agreement with the Picarro) and 17:00 (before LGR cavity temperatures began dropping).

191 A schematic diagram illustrating the sampling design for water vapour is shown in Figure 2. Half-
192 hourly vertical profiles of humidity and isotopes were sampled by drawing air to the *in-situ*
193 analyser through 10 mm O.D. PTFE tubing, located at 5 heights on a 7.5 m tower (0.5, 1, 2, 5 and
194 7.5 m Above Ground Level). The instrument was interfaced to a 5 inlet manifold that enabled
195 sequential sampling of the different heights. Approximately 20 m of tubing was required to connect
196 the tower inlet to the analyser. A vacuum pump (MV 2 NT, Vacuubrand, Wertheim, Germany)
197 was used to draw air through all inlets to the analyser at a flow rate of 10 l.min^{-1} , with the Picarro
198 bleeding off the 0.03 l.min^{-1} through its measurement cavity. To avoid condensation, sample tubes
199 and intakes were wrapped in 15 W m^{-1} heat tape, insulated by Thermobreak pipe and placed inside
200 100 mm PVC pipe. The sample tube temperature was controlled using a Resistance Thermometer
201 Detector (RTD) coupled to a CAL3300 temperature controller (CAL controls Ltd., Grayslake, IL,
202 USA). The inlets at each height were constructed from inverted funnels with mesh filters. In this
203 study we present block hourly averages of all measurements collected at all heights.

204 **2.2.2 Flux chambers**

205 To separate the isotopic signatures of the ET flux components, flux chambers were deployed on
206 both bare soil and vegetated plots to determine the isotopic signature of the evaporative fluxes. An
207 open chamber was designed with a high volume to footprint ratio to avoid the chamber mixing
208 ratio rapidly reaching the dew point temperature (causing condensation) and to minimise impacts
209 on the evaporation environment. A schematic of the chamber design is shown in Figure 3. Four
210 flanged metal collars were inserted $\sim 10 \text{ cm}$ into the soil column two days before the beginning of
211 the campaign. While this was a short settling time for chamber bases, shallow roots of grass cover
212 within the chamber were largely unaffected. All vegetation was removed from bare soil plots when

213 the metal collars were inserted into the soil. A single chamber cover was constructed of 4 mm G-
214 UVT Plexiglass (Image Plastics, Padstow, Australia), selected for its higher transmittance of UV
215 and blue light. The dimensions of the chamber were 0.1 x 0.1 x 0.8 m (width x length x height),
216 with the inlets and outlets at 0.1 and 0.7 m above the surface, respectively. All sampling tube was
217 10 mm PTFE. The inlet to the chamber was connected to tubing that drew in air from 1.5 m above
218 the ground surface. The outlet was connected to a flowmeter (VFA-25, Dwyers, Michigan City,
219 IN, USA) that regulated the air flow at $10 \text{ l}\cdot\text{min}^{-1}$ and was driven by a two-stage diaphragm pump.
220 A T-piece was connected to the LGR, which bled off approximately $0.8 \text{ l}\cdot\text{min}^{-1}$. All tubing between
221 chamber and the analyser were wrapped in heating tape (15 W m^{-2}) and foam insulation. High flow
222 rates were used to combat memory effects modifying the isotopic composition of the vapour within
223 the chamber. Analysis of chamber measurements were conducted on 2-5 minutes of data, so 2.5-
224 6.25 chamber volumes were exchanged.

225 To monitor the internal chamber environment, an air temperature and humidity probe (HMP155,
226 Vaisala, Vantaa, Finland) was mounted inside the chamber. To monitor the attenuation of the
227 incoming radiation by the chamber, photosynthetic flux density was measured (LI-190R, Licor,
228 Lincoln, NE, USA) inside and outside the chamber. Ten second averages of the temperature,
229 relative humidity and photosynthetic flux density were stored in a datalogger (CR1000, Campbell
230 Scientific, Logan, UT, USA). In the supplementary section we use these ancillary measurements
231 to assess the impact of observed changes in chamber environment on the isotopic composition of
232 the ET flux. The largest contributor to uncertainty caused by changing the evaporative
233 environment was the temperature, although these affects were small compared to the overall
234 variability of the chamber derived ET isotopic compositions.

235 2.2.3 Isotopic composition of ET flux from chamber measurements

236 Mass balance or Keeling mixing (Keeling, 1958; Wang et al. 2013) models have been applied to
237 determine the isotopic composition of ET fluxes from chamber measurements (Lu et al., 2016;
238 Wang et al., 2013b). The focus of this work was not to evaluate chamber measurement techniques.
239 Considering that it has been shown that Keeling and mass balance methods give very similar
240 results (Lu et al., 2016; Wang et al., 2013b) we focus on using the Keeling mixing model, given
241 by

$$242 \delta_{chamber} = q_{BG} \frac{(\delta_{BG} - \delta_{ET})}{q_{chamber}} + \delta_{ET} \quad (2)$$

243 where q_{BG} is the water vapour mixing ratio entering the chamber through the inlet and δ_{BG}
244 its isotopic composition, $q_{chamber}$ is the mixing ratio in the chamber and δ_{ET} is the isotopic
245 composition of the ET flux. The δ_{ET} is determined from the intercept of $\delta_{chamber}$ against $1/q_{chamber}$.
246 A key assumption of the Keeling method is that the isotopic composition of the background vapour
247 and the evaporation flux remain constant during the chamber measurements. For chamber
248 measurements longer than 5 minutes, non-linear Keeling plots were commonly observed,
249 indicating a change in isotopic composition of one of the sources of vapour. We therefore restricted
250 the Keeling analysis to a maximum of 5 minutes after an increase in the concentration was
251 observed by the analyser. Ensuring the linearity of Keeling plots also ensured that the influence of
252 memory effects was minimised. Memory effects would constitute an additional moisture source,
253 violating the two source assumption of the Keeling methods and reducing Keeling plot linearity.
254 The analysis was also restricted to periods where the H_2O mixing ratio was increasing, so analysis
255 was generally performed on 2-5 minutes of data. In addition, only chamber measurements where
256 the correlation between $\delta_{chamber}$ and $1/q_{chamber}$ was significant ($p < 0.001$) were included in this

257 analysis. A few chamber measurements where obvious non-linearity or very small changes in
 258 q_{chamber} occurred were also subjectively removed. Of a total of 105 chamber measurements made
 259 from the 4 vegetation plots during the campaign, 99 measurements of the $^2\text{H}_{\text{ET}}$, and 97
 260 measurements of $^{18}\text{O}_{\text{ET}}$ and d_{ET} were retained. For the bare soil plots, 84 of the 86 chamber
 261 measurements were retained for the $^2\text{H}_{\text{ET}}$, and 77 of the $^{18}\text{O}_{\text{ET}}$ and d_{ET} . The eight plots were
 262 sampled 2 to 4 times each day on all days except the first two days of the campaign, and the 2nd
 263 and 5th of May. Sampling was restricted to between 9:00 and 17:00 LST (local solar time) as the
 264 large temperature dependence of the LGR at low ambient temperatures limited the accuracy of the
 265 chamber measurements.

266 Results from vegetated plots were used to determine ET flux isotopic compositions and determine
 267 how ET influences d_v . The bare soil plots were used to determine the isotopic composition of soil
 268 evaporation fluxes and to provide an estimate of the isotopic composition of water at the
 269 evaporation front. The isotopic composition of the water at the evaporation front (δ_L) was
 270 determined by rearranging the Craig and Gordon model:

$$271 \quad \delta_L = \frac{\delta_E(1-RH)+RH \delta_A+\varepsilon+\varepsilon_k}{\alpha} \quad (3)$$

272 where the isotopic composition of the evaporation flux (δ_E) is taken from the bare soil
 273 chamber measurements, relative humidity (RH) normalised to the surface temperature determined
 274 from infrared surface temperature measurements (section 2.3), and the ambient vapour isotope
 275 composition (δ_A) determined from Picarro *in-situ* measurements. Equilibrium fractionation and
 276 enrichment factors (ε , $\varepsilon = (-1)\text{‰}$) were calculated from the surface temperature measurements
 277 using the equations of Horita and Wesolowski (1994), while the kinetic enrichment factor (ε_k) was

278 determined as in Gat (1996), but using the parameterisation of the exponent of the diffusion
279 coefficients described by Mathieu and Bariac (1996) and the diffusion coefficients determined by
280 Merlivat (1978).

281 **2.2.4 Iso-Forcing of ET**

282 The isotopic composition of the near-surface atmospheric water vapour is modified by surface ET
283 fluxes. The impact of ET fluxes on surface vapour isotopes varies over diurnal timescales with the
284 strength of vertical mixing in the ABL or over synoptic timescales as background moisture
285 conditions change. The magnitude and isotopic composition of the ET flux as well as the amount
286 of water vapour in the atmosphere also have an influence. The ET iso-forcing (I_{ET}) represents a
287 useful quantity to study the influence of ET fluxes on the surface vapour and is defined as:

$$288 \quad I_{ET} = \frac{F_{ET}}{H_2O} (\delta_{ET} - \delta_A) \quad (8)$$

289 where F_{ET} is the ET flux in $\text{mol}\cdot\text{m}^{-2}\cdot\text{s}^{-1}$, H_2O is the ambient mixing ratio in $\text{mol}\cdot\text{air}\cdot\text{mol}^{-1}$
290 H_2O^{-1} measured by the local meteorological tower, and δ_{ET} and δ_A are the isotopic compositions
291 of the evaporation flux and ambient water vapour, respectively (Lee et al. 2009).

292 For each chamber measurement, a surface iso-forcing was calculated for $\delta^2\text{H}$, $\delta^{18}\text{O}$ and D-excess
293 from the determined ET isotopic composition, as well as the hourly averaged ET flux, mixing ratio
294 and δ_A values. The importance of surface fluxes modifying surface vapour isotope composition
295 was investigated for diurnal and synoptic timescales.

296 **2.2.5 Plant and soil sampling**

297 Grass samples were collected three times a day for the duration of the campaign. They were
298 sampled randomly within 100 m of the instrumentation. Each sample consisted of approximately
299 10 grass leaves, which were placed in 12 ml Exetainer vials (Labco, Ceredigion, UK). The grass
300 samples were assumed to represent bulk leaf water. Soil samples were collected every 2 days
301 throughout the campaign by sampling from the top 5 cm of the soil column. They were collected
302 in 50 ml glass bottles. Soil and plant samples were stored in a fridge (4°C), before using the
303 distillation method of West *et al.* [2006] to extract liquid water samples that were analysed on a
304 Delta V Advantage Isotope Ratio Mass Spectrometer (Thermo Fisher Scientific Corporation,
305 Massachusetts, United States). For ^2H analysis, water samples were introduced into a H-Device
306 containing a chromium reactor, while for the ^{18}O analysis, water samples were equilibrated with
307 CO_2 on a Gas Bench II chromatography column (Thermo Fisher Scientific Corporation,
308 Massachusetts, USA) before being transferred to the IRMS for analysis.

309 **2.3 ET Fluxes and Meteorological measurements**

310 To measure ET fluxes, an eddy covariance system comprising a Campbell Scientific 3D sonic
311 anemometer (CSAT-3, Campbell Scientific, Logan, UT, USA) along with a LiCOR 7500 (Li-
312 7500, LiCor Biosciences, Lincoln, NB, USA) analyser was installed at an elevation of 2.5 m. The
313 system was located approximately 10 m from the stable isotope observation tower and sampled at
314 10 Hz, with flux averages output at 30 minute intervals. The ET fluxes from the eddy covariance
315 tower are used to quantify the Iso-Forcing of ET on the overlying atmosphere.

316 A meteorological tower was co-located with the eddy covariance system, providing
317 complementary data to aid in the interpretation of measurements. The tower comprised a Kipp and

318 Zonen CNR4 radiometer, Apogee infrared surface temperature, RIMCO rainguage, Vaisala
319 HMP75C temperature and humidity probe, RM Young wind sentry (wind speed and direction),
320 Huskeflux ground heat flux plate and Vaisala BaroCap barometric pressure sensor. Both
321 meteorological tower data and eddy-covariance data were inspected visually to detect and remove
322 spikes. The low-frequency eddy covariance data (30 minute resolution) were corrected for
323 coordinate rotation (Finnigan et al. 2003) and density effects (Leuning, 2007) using the PyQC
324 software tool (available from code.google.com/p/eddy).

325 **2.4 Radon-222 measurements**

326 The naturally occurring radioactive gas radon (^{222}Rn) is predominantly of terrestrial origin and its
327 only atmospheric sink is radioactive decay (Zahorowski et al. 2004). The surface flux density of
328 radon is relatively constant in space and time, and since the half-life is much greater than ABL
329 mixing timescales, it is an ideal tracer of vertical mixing strength within the ABL (Chambers et al.
330 2014; Griffiths et al. 2013; Williams et al. 2010). Hourly radon concentrations were measured by
331 an Alpha Guard (Saphymo GmbH, Frankfurt, Germany) placed in a ~20 L enclosure. The
332 enclosure was purged at $\sim 15 \text{ l}\cdot\text{min}^{-1}$ with a vacuum pump (2107 Series, Thomas, Wisconsin, USA)
333 that sampled from a height of 2 m through 10 mm O.D. PTFE tubing. Radon measurements were
334 used to aid the interpretation of the diurnal variations in vertical mixing (see Griffiths et al. 2013).

335 **3 Results**

336 **3.1 Meteorological observations**

337 The two-week campaign was conducted under predominantly calm meteorological conditions. The
338 last rain event was 10 days prior to the campaign, after which clear skies saw the soil dry to a
339 moisture content close to minimum values observed for the site (Figure 4). In the middle of the

340 campaign (May 2nd), a cold front moved across south eastern Australia, producing cloudy
341 conditions and 1.4 mm of precipitation at the site. No change in soil moisture was observed over
342 the 0-10 cm soil layer following the rain event.

343 Wind directions were variable during the campaign (see figure S2a and b). Figure S3 shows that
344 from 27th to 30th April, dominant daytime wind directions were mainly from the east. After May
345 3rd winds were from the south, except on the 7th and 8th when the wind was from the west and
346 had a fetch from the adjacent forest. At other times the fetch did not overlap the forested site. Daily
347 maximum temperatures on clear days ranged from 16 to 23°C, whilst night time minimum
348 temperatures fell to between 8 and -4°C. From May 7th onwards nocturnal temperatures fell below
349 zero. On clear nights the surface temperature fell below dew point temperature, indicating dew
350 fall. Apart from the night of the 27-28th April and the cloudy nights between 1st and 3rd May, the
351 surface temperature fell below dew point temperature and dew or frost was observed in the
352 morning, although heavier from the 7th May onwards.

353 Radon concentrations were low during the day, when the convective boundary layer reached its
354 maximum height, and high at night, when radon emissions were confined within the shallow
355 nocturnal boundary layer. The accumulation at night was variable indicating a varying degree of
356 nocturnal stability, mixing depth and occurrence of transient mixing events (Griffiths et al. 2013).
357 There was general agreement between high nocturnal radon concentrations and low wind speeds,
358 but no direct relationship. The lack of a direct relationship indicates that radon can provide
359 additional information about nocturnal mixing and surface exchange that compliments standard
360 meteorological measurements (Chambers et al. 2015a, 2015b; Williams et al. 2013).

361 ET fluxes were in general quite low, reflecting the low soil moisture content. The ET flux did show
362 a marked increase the day after the small rain event on May 2nd and noticeably smaller fluxes
363 were observed after the first night frost was observed. The health of the grass visibly deteriorated
364 from the 7th May, coinciding with frost formation.

365 **3.2 Relationship between ^2H and ^{18}O of the different water pools**

366 A summary of the isotopic composition of all observed and modelled water pools are presented
367 in Figure 6. The local MWL (Hughes and Crawford, 2013) is to the left of the global MWL (Craig,
368 1961), illustrating the characteristically high D-excess of precipitation in the region (Crawford et
369 al., 2013). Ambient vapour observations aligned closely with the local MWL, but with a
370 distribution that fell both to the left and right of the local MWL. Alignment between observations
371 and the MWL show that equilibrium fractionation was the dominant process modifying $\delta^2\text{H}$ and
372 $\delta^{18}\text{O}$ in water vapour, while non-equilibrium kinetic processes shift observations away from the
373 MWL and are more easily observed for d_v measurements.

374 Plant and soil water pools were enriched relative to the vapour and distributed to the right of the
375 MWL, indicating evaporative enrichment. Soil water isotopes at the evaporation front (u_L) were
376 very enriched and had lower D-excess values (50 ± 12 , 31 ± 3.8 and -131 ± 22 ‰ for $\delta^2\text{H}$, $\delta^{18}\text{O}$ and
377 D-excess) relative to the average soil moisture between 0 and 5 cm (-15 ± 4.2 , 2.6 ± 2.5 and -36 ± 17
378 ‰ for $\delta^2\text{H}$, $\delta^{18}\text{O}$ and D-excess). Low D-excess and enriched isotopes indicated large evaporative
379 enrichment under non-equilibrium conditions consistent with ^{18}O soil profile measurements of
380 Dubbert *et al.*, (2013) and ^2H profiles of Allison *et al.*, (1983). The uncertainty of modelled
381 isotope values was most sensitive to parameterisation of the Craig-Gordon model. Changing the
382 diffusion coefficient exponent (n) had the greatest impact on modelled soil water ($n=0.66$, 42.7 ± 12 ,

383 21.8±3.8 and -130.8±22 ‰). However, changing parameterisation did not change the conclusion
384 that soil moisture at the evaporation front was heavily enriched with very low D-excess values.

385 ET flux isotopic compositions from vegetated chambers were enriched relative to vapour and
386 distributed to the right of the MWL (slope = 3.2). Similar isotopic compositions were measured
387 from bare soil and vegetated chambers. Mean and standard deviations (1 σ) for vegetated and soil
388 chambers were -47.1 (±13) and -50.2 (±11) for ^2H , -5.03 (±3.8) and -6.3 (±2.7)‰ for ^{18}O , and -
389 6.3 (±23) and -0.12 (±15)‰ for D-excess, respectively. The similar ET isotopic composition from
390 bare soil and vegetated chambers could indicate soil evaporation was the dominant process
391 contributing to total ET. However, as pointed out in the discussion (section 4.3), convergence of
392 soil evaporation and transpiration isotope compositions as the soil evaporation source becomes
393 progressively enriched (and D-excess lower), probably makes it difficult to identify the dominant
394 process from these observations. Nevertheless, since the last significant rain event prior to the
395 campaign, progressive reduction of D-excess of moisture at the evaporation front and to a lesser
396 extent in the 0-5 cm layer caused low D-excess of overall ET fluxes compared to d_v . This would
397 indicate that ET imposes a negative forcing on d_v .

398 Temporally, a clear trend was not observed for ET isotopic compositions over the measured
399 portion of the diurnal cycle or over the campaign. No measurements were made at night or during
400 the rapidly changing conditions of the morning transition, which may have led to our data missing
401 some observed changes in ET isotope compositions.

402 **3.3 *In-situ* water vapour isotopes and ET iso-forcing**

403 Observed water vapour mixing ratios and stable isotope compositions are shown in Figure 7. ^2H
404 and ^{18}O variability was similar, reflecting changes in both the synoptic and local meteorology.

405 Prior to the rain event (May 2nd), relatively moist conditions (higher H₂O mixing ratios) were
406 observed as air was transported from the warmer ocean off the east coast of Australia (see wind
407 direction in figure S3). After May 5th, transport of air masses from the colder sea surface south of
408 continental Australia brought drier conditions to the site (lower H₂O mixing ratios). Moisture
409 source regions were confirmed by backward air trajectories calculated using the Stochastic Time-
410 Inverted Lagrangian Transport Model (STILT; Lin *et al.* (2003) not shown). These two time
411 periods are hereinafter referred as “wet period” (before May 2nd) and “dry periods” (after May
412 5th). The wet period coincided with more enriched isotopes and less diurnal variability. In the later
413 part of the campaign, a reproducible diurnal cycle for ²H and δ¹⁸O was observed (see Figure 8
414 for diurnal composites), presenting a sharp increase at sunrise before decreasing from mid-morning
415 (when vertical mixing increased) until the next sunrise. These observations emphasise the complex
416 relationship between stable isotope observations in water vapour and both local and synoptic scale
417 meteorology.

418 The d_v dataset showed a robust diurnal cycle of high values in the day and low values at night,
419 consistent with what has been observed across a growing number of locations (Bastrikov *et al.*
420 2014; Berkelhammer *et al.* 2013; Simonin *et al.* 2014; Welp *et al.* 2012; Zhao *et al.* 2014). Wet
421 period daytime d_v values were on average lower than those observed for the dry period. Nocturnal
422 d_v was consistently lower during the night, but variable from night to night and across individual
423 nights, with no clear difference observed between wet and dry periods. Contrasting daytime
424 measurements of wet and dry periods indicate a role of large scale processes, whilst the lack of
425 contrast for nocturnal observation show the importance of local processes.

426 The I_{ET} was always positive for 2H and ^{18}O and mostly negative for D-excess, but showed large
427 variability across individual days (Figure 7). I_{ET} was most sensitive to the magnitude of the ET
428 fluxes, producing the greatest forcing on ambient vapour in the middle of the day. The I_{ET} time
429 series did not correspond to temporal variability of vapour 2H , $\delta^{18}O$ or D-excess. 2H and ^{18}O
430 often decreased during the day while I_{ET} was positive. Whilst the high d_v values observed during
431 the day were associated with negative isoforcing, over the course of the campaign highest daytime
432 d_v values did not correspond to the least negative I_{ET} . These observations illustrate that local ET
433 fluxes were not overly important for day-to-day and diurnal d_v trends.

434 The level of agreement between the analysers presented some uncertainty for calculation of the D-
435 excess isoforcing. The sign of the isoforcing is dependent on the difference between d_v and d_{ET}
436 (equation 8). In some cases this difference was small and within the range of agreement between
437 the two analysers. While this caused problems for accurate calculation of the absolute values of
438 D-excess isoforcing, for all chamber measurements passing our QC requirements, D-excess
439 decreased with concentration. This indicates that for all measurements the D-excess, isoforcing
440 was negative.

441 **3.4 Relationship between water vapour isotopes and local meteorology**

442 The relationships between local meteorological variables and water vapour isotopes were
443 examined to interpret the role of local processes (Table 1). Regression statistics are shown for both
444 hourly observations and average daytime values (between 11:00 and 16:00 LST). Selecting
445 daytime measurements removes variability associated with transition between the stable nocturnal
446 and daytime convective boundary layer, as well as nocturnal periods when local surface
447 equilibrium exchange and dewfall affect vapour isotope compositions. Correlations determined

448 using only measurements in the middle of the day therefore provide a better indicator of how local
449 meteorology and ET isotopic composition modified ambient water vapour isotope ratios from day
450 to day.

451 Correlations calculated with hourly data were weak for ^{18}O and ^2H . Only correlations with air
452 temperature ($R^2=0.24$ and 0.04 , respectively) and mixing ratio ($R^2=0.2$ for both isotopes) were
453 significant, and ^2H also showed a weak correlation with RH ($R^2=0.09$). For daytime observations,
454 only ^2H showed a significant correlation with daytime I_{ET} ($R^2=0.45$, $p<0.05$), but the slope was
455 negative in contrast to positive isoforcing. The weak relationships with local meteorology indicate
456 the importance of larger scale precipitation processes and atmospheric mixing occurring as
457 moisture was transported to the site.

458 As the diurnal cycle for d_v was consistent with growth and decay of the ABL, strong relationships
459 were observed with air temperature and RH for the hourly observations. While the local air
460 temperature and RH could modify d_{ET} on diurnal timescales and in turn local d_v , the chamber
461 measurements showed relatively constant d_{ET} . These correlations therefore result from the
462 coincident diurnal variation of the d_v , RH and air temperature.

463 Daytime average d_v showed significant correlations with the air temperature, RH, ET flux and
464 mixing ratio. The relationship with ET fluxes was weak ($R^2=0.3$) and positive, but as negative D-
465 excess isoforcing was observed, a negative relationship would be expected. Likewise, the slope
466 between air temperature and d_v was negative, counter to what theory would predict for local or
467 remote moisture sources. The strongest relationship was observed with daytime RH ($R^2 = 0.74$),
468 which had a negative slope ($-0.52\%.\%^{-1}$) consistent with an inverse relationship between d_v and

469 RH for a large unchanging evaporation source. The strong relationship of d_v with the daytime RH
470 could indicate an important role for the evaporation conditions at remote moisture sources, as is
471 discussed below in Section 4.2.

472 **3.5 Diurnal variability of vapour isotopes**

473 Diurnal composites were divided into dry and wet periods and are shown in Figure 8. At sunrise
474 (approximately 06:30 LST) surface heating initiated vertical mixing, shown by the radon
475 concentration maximum, causing temperature and ET flux to increase and RH decrease. Weak
476 vertical mixing immediately after sunrise and injection of ET into the still shallow surface layer
477 caused near-surface humidity to increase. Similarly for ^2H and $\delta^{18}\text{O}$, the observed spike
478 immediately after sunrise was likely caused by ET fluxes with an enriched heavy isotope
479 composition, possibly from re-evaporation of dewfall. During the dry period, vapour ^2H and $\delta^{18}\text{O}$
480 increased more steeply, caused by the combination of a shallower surface layer observed at the
481 start of the morning transition, shown by higher radon concentrations, and more dewfall on the
482 surface providing a greater initial evaporation source. Rapidly decreasing radon concentrations
483 during this morning ABL transition caused by vigorous vertical mixing entraining air from the
484 residual layer of the previous day diluted ET fluxes and caused the ^2H , $\delta^{18}\text{O}$ and the mixing ratio
485 to first stabilise and then decrease. ET fluxes rapidly increased as the ABL grew, but were not
486 large enough to offset the dilution by dry air being mixed down from above or stop depletion of
487 surface ^2H and ^{18}O .

488 The d_v also increased after sunrise, but aligned more closely to when strong vertical mixing
489 commenced, as shown by the close agreement with radon concentrations. The D-excess isoforcing
490 was negative, evidence that d_v increased from encroachment mixing as the new mixed layer grew

491 in depth and not ET fluxes. The dry period showed a greater increase in d_v during the morning
492 transition, likely the result of higher d_v in background water vapour and greater differences
493 between the d_v of the residual and nocturnal layer.

494 In the afternoon, d_v decreased back to values similar to those observed prior to sunrise, with a
495 simultaneous decrease in solar insolation, ET and a decay of convective mixing. Radon shows how
496 reduction in vertical mixing causes the concentration of tracers emitted from the surface to
497 increase. So while ET decreased, small fluxes were still observed well after 18:00, when large
498 changes in ^{18}O and d_v were observed. Hence, as the I_{ET} was positive and negative for ^{18}O and
499 D-excess, respectively, small ET fluxes into a poorly mixed surface layer may have led to observed
500 changes.

501 During the night, dew fall caused ^2H and ^{18}O to decrease as heavy isotopes were removed in
502 condensation, especially during the dry period when greater surface cooling was observed.
503 However, dew formation is an equilibrium processes so did not affect d_v . Composites of dry and
504 wet period nocturnal d_v measurements do not show clear nocturnal trends, but individual nights
505 showed considerable variability. A regression of nocturnal d_v with radon concentrations produced
506 a significant negative relationship ($p < 0.001$, $R^2 = 0.31$), indicating that atmospheric stability has
507 some control over nocturnal d_v . High radon is associated with the most stable atmospheres,
508 enhancing the effect of surface exchange in the early evening. Low radon on the other hand, is
509 associated with periods of atmospheric turbulence in which moisture above the nocturnal inversion
510 with a high d_v is mixed down towards the surface.

511

512 4 Discussion

513 As has been previously observed (Steen-Larsen et al. 2013; Welp et al. 2012) and predicted by
514 isotopic models (Gat, 1996), our observations showed water vapour ^2H and ^{18}O are controlled
515 by different atmospheric and hydrological processes than d_v . The diurnal cycle was the dominant
516 mode of variability for d_v , consistent with previous studies for a range of ecosystems (Simonin et
517 al. 2014; Welp et al. 2012; Zhao et al. 2014). However, results also showed that D-excess
518 variability was controlled by local meteorological conditions and surface exchange at night, ABL
519 growth and decay during transitional periods between the nocturnal and convective ABL, and
520 larger scale processes in the middle of the day.

521 4.1 Entrainment and the d_v diurnal cycle

522 The radon measurements showed that when the depth of the ABL was rapidly changing through
523 the morning and evening transitions, entrainment from the residual layer and ET fluxes into a
524 rapidly decaying convective boundary layer caused the observed d_v diurnal cycle. Between these
525 transitions, when mixing extends to the capping inversion, entrainment fluxes introduce an
526 additional moisture source from the free troposphere that could modify surface vapour isotopic
527 compositions. Air above the ABL is drier and moisture is more depleted than at the surface. Drying
528 and depleting trends for water vapour, ^2H and ^{18}O throughout the day, particularly during the
529 dry period (Figure 8), indicate an important role for entrainment from the free troposphere.
530 Whether this moisture flux impacts on d_v is less clear, as it remained reasonably stable once a
531 maximum was reached after the morning transition period. The sign of the isoforcing of moisture
532 entrained from the free troposphere is uncertain, as few free tropospheric d_v measurements exist
533 (He and Smith, 1999; Samuels-Crow et al., 2014). Nevertheless, d_v values did not show a clear

534 trend until vertical mixing began decaying later in the afternoon, so free tropospheric d_v probably
535 has a similar value to moisture already residing in the ABL.

536 **4.2 Remote hydrometeorological processes**

537 While the main focus of this study was to examine the role of local land-atmosphere exchange for
538 the diurnal variability of d_v , the synoptic context of measurements warrants further examination
539 for comparison against previous studies of d_v diurnal cycles. The slope between daytime RH and
540 d_v ($-0.52\%.\%^{-1}$, Table 1) was similar to those determined for measurements over the
541 Mediterranean sea and different ocean basins (between -0.43 and $-0.53\%.\%^{-1}$) (Kurita, 2011;
542 Pfahl and Wernli, 2008; Steen-Larsen et al. 2014, 2015; Uemura et al. 2008). Aemisegger *et al.*
543 (2014) showed that this robust relationship is not restricted to coastal locations or measurements
544 over the ocean surface. Using a trajectory model to investigate continental moisture recycling in
545 Europe, they found a similar relationship between d_v and RH of remote moisture sources during
546 the cold season ($-0.57\%.\%^{-1}$), but not for warm season observations. They concluded moisture
547 recycling is weakest during winter, causing d_v to retain the signature of the RH of oceanic moisture
548 sources, while in summer moisture recycling increased and attenuated the relationship. Similarities
549 with their winter data indicates that our daytime d_v measurements were at least partly determined
550 by RH at the oceanic moisture source.

551 Along an air masses back trajectory, entrainment fluxes from the free troposphere could be a major
552 driver of daytime d_v variability. Mixing of warm dry air down to the surface, presumably with a
553 relatively high D-excess (He and Smith, 1999; Samuels-Crow et al., 2014), would give the same
554 negative relationship between d_v and RH observed here. However, for a strong relationship
555 between d_v and RH, there must be a dominant moisture source. For the fraction of entrained air in

556 the ABL to cause the strong linear relationship, the D-excess of vapour and RH in both the ABL
557 and free troposphere must be reasonably constant, as in a two source mixing model. Considering
558 the variability of synoptic scale weather patterns observed (section 3.1), this seems unlikely. Thus,
559 while we cannot definitively rule out the importance of entrainment along back trajectories, it
560 seems more likely that the d_v vs RH relationship was derived from a large unchanging moisture
561 source such as the ocean.

562 A practical application of the d_v /RH relationship introduced by Aemisegger *et al.* (2014) was to
563 determine the D-excess of the liquid moisture source. Based on the closure assumption of Merlivat
564 and Jouzel (1979), it was shown when RH is 100%, d_v is equal to the D-excess of the liquid
565 moisture source. If no further kinetic fractionation or mixing of vapour with a different d_v /RH
566 occurred between the point of evaporation and measurement location, extrapolating the regression
567 between d_v and RH to 100% RH gives an estimate of moisture source D-excess. For our
568 measurements, a value of -8‰ was determined, remarkably similar to the D-excess determined for
569 ocean water off the east coast of Australia by Xu *et al.* (2012) using a global ocean model. In
570 contrast to recent literature (Simonin *et al.* 2014; Welp *et al.* 2012; Zhao *et al.* 2014), this suggests
571 that although the common diurnal cycle was observed, daytime observations are potentially a
572 tracer of RH at the oceanic moisture source, but it is likely restricted to periods when moisture
573 recycling is weak.

574 Whilst we have shown a relationship between the RH and d_v consistent with an oceanic vapour
575 source, the consistency of the relationship over longer time periods is uncertain. Indeed, it may be
576 the reason why we show a strong relationship whereas the study of Welp *et al.* (2012) did not for
577 six mid-latitude sites in China and the USA, where longer datasets were available. As pointed out

578 earlier, lowers slopes and weaker relationships result from stronger moisture recycling, which
579 indicates moisture recycling and soil moisture state may be the most important variable controlling
580 the relationship between d_v and RH. Here we present data from after an extended dry period, where
581 the dominant moisture source is the ocean surrounding the Australian continent. So during wetter
582 periods, increase in the local and remote moisture recycling probably weaken the relationship
583 between local d_v and RH (Aemisegger et al. 2014). However, for locations such as semi-arid
584 Australia where extended dry periods prevail, the relationship between d_v and RH may be
585 reasonably robust and prevail as a tracer of oceanic evaporative environments.

586 **4.3 Controls of d_{ET}**

587 The chamber d_{ET} measurements showed ET fluxes imposed a negative isoforcing on d_v , in contrast
588 to interpretations in previous studies investigating d_v variability on diurnal time scales (Simonin et
589 al. 2014; Zhao et al. 2014). However, it is expected that the sign and magnitude of the D-excess
590 isoforcing would vary both spatially and temporally, in particular with soil moisture state. After a
591 rain event, soil moisture D-excess would decrease following a pseudo-Rayleigh process (Barnes
592 and Allison, 1988). Therefore, immediately after a rainfall event, d_{ET} would be higher and probably
593 impose a positive isoforcing. Here the negative d_{ET} caused the d_v to decrease rapidly as convective
594 mixing shut down. When isoforcing is positive after a rain event, the diurnal cycle observed here
595 and elsewhere may therefore not be observed. Although equilibration between liquid and vapour
596 pools, as eluded to by Simonin *et al.*, (2014), may still help maintain observed trends. As soil dries,
597 a tipping point when the ET fluxes switch from positive to negative isoforcing will be observed.
598 This has implications for studies attempting to use d_v as a tracer of continental moisture recycling,
599 as the large spatial variability of rainfall and the associated soil moisture state would lead to large

600 spatial and temporal variability for d_{ET} . Although, the strongest moisture recycling is expected for
601 wet soils when d_{ET} is higher, variability in d_{ET} may still be important.

602 Relative magnitudes of evaporation and transpiration fluxes are important for d_{ET} , as the two
603 processes could have different D-excess values and could vary strongly between precipitation or
604 irrigation events. The classical view of ET isotope fluxes is that transpiration has an isotopic
605 composition closer to the source moisture than evaporation, so a higher D-excess. However,
606 greater fractionation of the evaporation source pool causes its D-excess value to decrease over
607 time, so the D-excess of the fluxes would converge overtime. The impact of converging isotopic
608 signatures of ET component fluxes on moisture recycling would depend on the land surface type,
609 but would constitute an important variable influencing the D-excess of local and remote moisture
610 recycling. Further studies investigating how ET partitioning and drying of soil moisture reservoirs
611 following irrigation or precipitation events would lead to a better understanding of how moisture
612 recycling influences the ambient d_v on continental and local scales.

613 **5 Conclusions**

614 To determine how local ET fluxes modified water vapour D-excess, in-situ observations were
615 collected in a semi-arid region of south-eastern Australia. The diurnal cycle exhibited high values
616 during the day and low values at night, reflected findings from previous studies. With chamber
617 based measurements of isotopic compositions in evaporative fluxes, it was shown that local ET
618 fluxes exhibited a negative forcing on the ambient water vapour D-excess that could not explain
619 the high daytime values. A strong negative relationship was observed between the locally
620 measured relative humidity and vapour D-excess during the daytime, consistent with relationships

621 observed for oceanic moisture sources. During the evening transition, collapse of the convective
622 boundary layer and small ET fluxes with negative D-excess isoforcing were responsible for
623 lowering the D-excess of water vapour near the surface. In addition, a negative nocturnal
624 correlation between D-excess in water vapour and radon concentrations indicated transient
625 nocturnal mixing events shifted the D-excess back towards the higher values observed during the
626 day, with the most stable (least turbulent) nights producing the lowest D-excess values. In the
627 morning, encroachment and entrainment of high D-excess air from above caused D-excess of
628 surface vapour to increase back to the synoptic values.

629 Overall, it was found that the magnitude of the D-excess diurnal cycle was controlled
630 predominantly by interplay between synoptic forcing and local ABL processes and was modified
631 further by nocturnal surface exchange processes and turbulent mixing. The low D-excess of the
632 ET fluxes determined from flux chambers in this study illustrated that the impact of large scale
633 moisture recycling may be both spatially and temporally variable, depending on the soil moisture
634 state. This has implications for studies using D-excess to investigate moisture recycling.

635 **6 Acknowledgements**

636 Stephen Parkes was supported by the Atmospheric Mixing and Pollution Transport (AMPT)
637 project at the Australian Nuclear Science and Technology Organization (ANSTO) and the King
638 Abdullah University of Science and Technology. The Baldry Hydrological Observatory field
639 campaign was supported by Australian Research Council Discovery grants DP0987478 and
640 DP120104718. Matthew McCabe acknowledges the support of the King Abdullah University of
641 Science and Technology. We thank Dr Peter Graham, Cecilia Azcurra, Dr. Jin Wang and Yingzhe
642 Cai for their assistance during the campaign. We also appreciate the support of Diana and Jason

643 Tremain for access to the Baldry Hydrological Observatory and surrounding farmland, Chris
644 Dimovski for performing plant and soil water extractions, and Barbara Neklapilova analysis of
645 plant and soil water samples.

646 For access to the data used in this paper contact Dr Stephen Parkes by email
647 (stephen.parkes@kaust.edu.sa).

648

649

650 **7 References**

651 Aemisegger, F., Pfahl, S., Sodemann, H., Lehner, I., Seneviratne, S. I. and Wernli, H.: Deuterium
652 excess as a proxy for continental moisture recycling and plant transpiration, *Atmos. Chem. Phys.*,
653 14(8), 4029–4054, doi:10.5194/acp-14-4029-2014, 2014.

654 Allison, G. B., Barnes, C. J. and Hughes, M. W.: The distribution of deuterium and ¹⁸O in dry
655 soils 2. Experimental, *J. Hydrol.*, 64(1-4), 377–397, doi:10.1016/0022-1694(83)90078-1, 1983.

656 Barnes, C. J. and Allison, G. B.: Tracing of water movement in the unsaturated zone using stable
657 isotopes of hydrogen and oxygen, *J. Hydrol.*, 100(1-3), 143–176, doi:10.1016/0022-
658 1694(88)90184-9, 1988.

659 Bastrikov, V., Steen-Larsen, H. C., Masson-Delmotte, V., Gribanov, K., Cattani, O., Jouzel, J. and
660 Zakharov, V.: Continuous measurements of atmospheric water vapour isotopes in western Siberia
661 (Kourovka), *Atmos. Meas. Tech.*, 7(6), 1763–1776, doi:10.5194/amt-7-1763-2014, 2014.

662 Berkelhammer, M., Hu, J., Bailey, A., Noone, D. C., Still, C. J., Barnard, H., Gochis, D., Hsiao,
663 G. S., Rahn, T. and Turnipseed, A.: The nocturnal water cycle in an open-canopy forest, *J.*
664 *Geophys. Res. Atmos.*, 118(17), 10,210–225,242, doi:10.1002/jgrd.50701, 2013.

665 Chambers, S. D., Wang, F., Williams, A. G., Xiaodong, D., Zhang, H., Lonati, G., Crawford, J.,
666 Griffiths, A. D., Ianniello, A. and Allegrini, I.: Quantifying the influences of atmospheric stability
667 on air pollution in Lanzhou, China, using a radon-based stability monitor, *Atmos. Environ.*, 107,
668 233–243, doi:10.1016/j.atmosenv.2015.02.016, 2015a.

669 Chambers, S. D., Williams, A. G., Crawford, J. and Griffiths, A. D.: On the use of radon for
670 quantifying the effects of atmospheric stability on urban emissions, *Atmos. Chem. Phys. Discuss.*,
671 14(18), 25411–25452, doi:10.5194/acpd-14-25411-2014, 2014.

672 Chambers, S. D., Williams, A. G., Crawford, J. and Griffiths, A. D.: On the use of radon for

673 quantifying the effects of atmospheric stability on urban emissions, *Atmos. Chem. Phys.*, 15(3),
674 1175–1190, doi:10.5194/acp-15-1175-2015, 2015b.

675 Craig, H.: Isotopic Variations in Meteoric Waters, *Sci.*, 133 (3465), 1702–1703,
676 doi:10.1126/science.133.3465.1702, 1961.

677 Craig, H. and Gordon, L. I.: Deuterium and oxygen-18 variations in the ocean and marine
678 atmosphere, in *Stable isotopes in oceanographic studies and paleotemperatures*, Proceedings,
679 Spoleto, Italy., edited by E. Tongiogi, pp. 9–130, Pisa, Italy., 1965.

680 Crawford, J., Hughes, C. E. and Parkes, S. D.: Is the isotopic composition of event based
681 precipitation driven by moisture source or synoptic scale weather in the Sydney Basin, Australia?,
682 *J. Hydrol.*, 507(0), 213–226, doi:http://dx.doi.org/10.1016/j.jhydrol.2013.10.031, 2013.

683 Dansgaard, W.: Stable isotopes in precipitation, *Tellus*, 16(4), 436–468, doi:10.1111/j.2153-
684 3490.1964.tb00181.x, 1964.

685 Decker, M., Pitman, A. and Evans, J.: Diagnosing the seasonal land–atmosphere correspondence
686 over northern Australia: dependence on soil moisture state and correspondence strength definition,
687 *Hydrol. Earth Syst. Sci.*, 19(8), 3433–3447, doi:10.5194/hess-19-3433-2015, 2015.

688 Dubbert, M., Cuntz, M., Piayda, A., Maguás, C. and Werner, C.: Partitioning evapotranspiration
689 – Testing the Craig and Gordon model with field measurements of oxygen isotope ratios of
690 evaporative fluxes, *J. Hydrol.*, 496, 142–153, doi:10.1016/j.jhydrol.2013.05.033, 2013.

691 Evans, J. P. and McCabe, M. F.: Regional climate simulation over Australia’s Murray-Darling
692 basin: A multitemporal assessment, *J. Geophys. Res. Atmos.*, 115(D14), n/a–n/a,
693 doi:10.1029/2010JD013816, 2010.

694 Finnigan, J. J., Clement, R., Malhi, Y., Leuning, R. and Cleugh, H. A.: A Re-Evaluation of Long-
695 Term Flux Measurement Techniques Part I: Averaging and Coordinate Rotation, *Boundary-Layer*
696 *Meteorol.*, 107(1), 1–48, doi:10.1023/A:1021554900225, 2003.

697 Froehlich, K., Kralik, M., Papesch, W., Rank, D., Scheifinger, H. and Stichler, W.: Deuterium
698 excess in precipitation of Alpine regions – moisture recycling, *Isotopes Environ. Health Stud.*,
699 44(1), 61–70, doi:10.1080/10256010801887208, 2008.

700 Gat, J. R.: OXYGEN AND HYDROGEN ISOTOPES IN THE HYDROLOGIC CYCLE, *Annu.*
701 *Rev. Earth Planet. Sci.*, 24(1), 225–262, doi:10.1146/annurev.earth.24.1.225, 1996.

702 Gat, J. R., Bowser, C. J. and Kendall, C.: The contribution of evaporation from the Great Lakes to
703 the continental atmosphere: estimate based on stable isotope data, *Geophys. Res. Lett.*, 21(7), 557–
704 560, doi:10.1029/94GL00069, 1994.

705 Gat, J. R., Klein, B., Kushnir, Y., Roether, W., Wernli, H., Yam, R. and Shemesh, A.: Isotope
706 composition of air moisture over the Mediterranean Sea: an index of the air–sea interaction pattern,
707 *Tellus B*, 55(5), 953–965, doi:10.1034/j.1600-0889.2003.00081.x, 2003.

708 Griffiths, A. D., Parkes, S. D., Chambers, S. D., McCabe, M. F. and Williams, A. G.: Improved
709 mixing height monitoring through a combination of lidar and radon measurements, *Atmos. Meas.*
710 *Tech.*, 6(2), 207–218, doi:10.5194/amt-6-207-2013, 2013.

711 Harding, K. J. and Snyder, P. K.: Modeling the Atmospheric Response to Irrigation in the Great
712 Plains. Part I: General Impacts on Precipitation and the Energy Budget, *J. Hydrometeorol.*, 13(6),

713 1667–1686, doi:10.1175/JHM-D-11-098.1, 2012.

714 He, H. and Smith, R. B.: Stable isotope composition of water vapor in the atmospheric boundary
715 layer above the forests of New England, *J. Geophys. Res. Atmos.*, 104(D9), 11657–11673,
716 doi:10.1029/1999JD900080, 1999.

717 Horita, J. and Wesolowski, D. J.: Liquid-vapor fractionation of oxygen and hydrogen isotopes of
718 water from the freezing to the critical temperature, *Geochim. Cosmochim. Acta*, 58(16), 3425–
719 3437, doi:http://dx.doi.org/10.1016/0016-7037(94)90096-5, 1994.

720 Huang, L. and Wen, X.: Temporal variations of atmospheric water vapor D and ¹⁸O above an
721 arid artificial oasis cropland in the Heihe River Basin, *J. Geophys. Res. Atmos.*, 119(19),
722 2014JD021891, doi:10.1002/2014JD021891, 2014.

723 Hughes, C. E. and Crawford, J.: Spatial and temporal variation in precipitation isotopes in the
724 Sydney Basin, Australia, *J. Hydrol.*, 489(0), 42–55,
725 doi:http://dx.doi.org/10.1016/j.jhydrol.2013.02.036, 2013.

726 Jana, R. B., Ershadi, A. and McCabe, M. F.: Examining the relationship between intermediate-
727 scale soil moisture and terrestrial evaporation within a semi-arid grassland, *Hydrol. Earth Syst.*
728 *Sci.*, 20(10), 3987–4004, doi:10.5194/hess-20-3987-2016, 2016.

729 Keeling, C. D.: The concentration and isotopic abundances of atmospheric carbon dioxide in rural
730 areas, *Geochim. Cosmochim. Acta*, 13(4), 322–334, doi:10.1016/0016-7037(58)90033-4, 1958.

731 Kurita, N.: Origin of Arctic water vapor during the ice-growth season, *Geophys. Res. Lett.*, 38(2),
732 n/a–n/a, doi:10.1029/2010GL046064, 2011.

733 Lai, C.-T. and Ehleringer, J.: Deuterium excess reveals diurnal sources of water vapor in forest air,
734 *Oecologia*, 165(1), 213–223, doi:10.1007/s00442-010-1721-2, 2011.

735 Lee, X., Griffis, T. J., Baker, J. M., Billmark, K. A., Kim, K. and Welp, L. R.: Canopy-scale kinetic
736 fractionation of atmospheric carbon dioxide and water vapor isotopes, *Global Biogeochem.*
737 *Cycles*, 23(1), GB1002, doi:10.1029/2008GB003331, 2009.

738 Leuning, R.: The correct form of the Webb, Pearman and Leuning equation for eddy fluxes of
739 trace gases in steady and non-steady state, horizontally homogeneous flows, *Boundary-Layer*
740 *Meteorol.*, 123(2), 263–267, doi:10.1007/s10546-006-9138-5, 2007.

741 Lin, J. C., Gerbig, C., Wofsy, S. C., Andrews, A. E., Daube, B. C., Davis, K. J. and Grainger, C.
742 A.: A near-field tool for simulating the upstream influence of atmospheric observations: The
743 Stochastic Time-Inverted Lagrangian Transport (STILT) model, *J. Geophys. Res.*, 108, 4493,
744 doi:10.1029/2002JD003161, 2003.

745 Lu, X., Liang, L. L., Wang, L., Jenerette, G. D., McCabe, M. F. and Grantz, D. A.: Partitioning of
746 evapotranspiration using a stable isotope technique in an arid and high temperature agricultural
747 production system, *Agric. Water Manag.*, In Press, ,
748 doi:http://dx.doi.org/10.1016/j.agwat.2016.08.012, 2016.

749 Masson-Delmotte, V., Jouzel, J., Landais, A., Stievenard, M., Johnsen, S. J., White, J. W. C.,
750 Werner, M., Sveinbjornsdottir, A. and Fuhrer, K.: GRIP Deuterium Excess Reveals Rapid and
751 Orbital-Scale Changes in Greenland Moisture Origin, *Sci.* , 309 (5731), 118–121,
752 doi:10.1126/science.1108575, 2005.

- 753 Mathieu, R. and Bariac, T.: A numerical model for the simulation of stable isotope profiles in
754 drying soils, *J. Geophys. Res. Atmos.*, 101(D7), 12685–12696, doi:10.1029/96JD00223, 1996.
- 755 McCabe, M. F., Ershadi, A., Jimenez, C., Miralles, D. G., Michel, D. and Wood, E. F.: The
756 GEWEX LandFlux project: evaluation of model evaporation using tower-based and globally
757 gridded forcing data, *Geosci. Model Dev.*, 9(1), 283–305, doi:10.5194/gmd-9-283-2016, 2016.
- 758 McCabe, M. F., Franks, S. W. and Kalma, J. D.: Calibration of a land surface model using multiple
759 data sets, *J. Hydrol.*, 302(1–4), 209–222, doi:http://dx.doi.org/10.1016/j.jhydrol.2004.07.002,
760 2005.
- 761 Merlivat, L.: Molecular diffusivities of H₂O₁₆O, HD₁₆O, and H₂¹⁸O in gases, *J. Chem. Phys.*,
762 69(6), 2864, doi:10.1063/1.436884, 1978.
- 763 Merlivat, L. and Jouzel, J.: Global climatic interpretation of the deuterium-oxygen 18 relationship
764 for precipitation, *J. Geophys. Res. Ocean.*, 84(C8), 5029–5033, doi:10.1029/JC084iC08p05029,
765 1979.
- 766 Noone, D., Risi, C., Bailey, A., Berkelhammer, M., Brown, D. P., Buening, N., Gregory, S.,
767 Nusbaumer, J., Schneider, D., Sykes, J., Vanderwende, B., Wong, J., Meillier, Y. and Wolfe, D.:
768 Determining water sources in the boundary layer from tall tower profiles of water vapor and
769 surface water isotope ratios after a snowstorm in Colorado, *Atmos. Chem. Phys.*, 13(3), 1607–
770 1623, doi:10.5194/acp-13-1607-2013, 2013.
- 771 Pfahl, S. and Wernli, H.: Air parcel trajectory analysis of stable isotopes in water vapor in the
772 eastern Mediterranean, *J. Geophys. Res. Atmos.*, 113(D20), n/a–n/a, doi:10.1029/2008JD009839,
773 2008.
- 774 Pfahl, S. and Wernli, H.: Lagrangian simulations of stable isotopes in water vapor: An evaluation
775 of nonequilibrium fractionation in the Craig-Gordon model, *J. Geophys. Res. Atmos.*, 114(D20),
776 D20108, doi:10.1029/2009JD012054, 2009.
- 777 Risi, C., Noone, D., Frankenberg, C. and Worden, J.: Role of continental recycling in intraseasonal
778 variations of continental moisture as deduced from model simulations and water vapor isotopic
779 measurements, *Water Resour. Res.*, 49(7), 4136–4156, doi:10.1002/wrcr.20312, 2013.
- 780 Samuels-Crow, K. E., Galewsky, J., Sharp, Z. D. and Dennis, K. J.: Deuterium-excess in
781 subtropical free troposphere water vapor: continuous measurements from the Chajnantor Plateau,
782 northern Chile, *Geophys. Res. Lett.*, 2014GL062302, doi:10.1002/2014GL062302, 2014.
- 783 Simonin, K. A., Link, P., Rempe, D., Miller, S., Oshun, J., Bode, C., Dietrich, W. E., Fung, I. and
784 Dawson, T. E.: Vegetation induced changes in the stable isotope composition of near surface
785 humidity, *Ecohydrology*, 7(3), 936–949, doi:10.1002/eco.1420, 2014.
- 786 Steen-Larsen, H. C., Johnsen, S. J., Masson-Delmotte, V., Stenni, B., Risi, C., Sodemann, H.,
787 Balslev-Clausen, D., Blunier, T., Dahl-Jensen, D., Ellehøj, M. D., Falourd, S., Grindsted, A.,
788 Gkinis, V., Jouzel, J., Popp, T., Sheldon, S., Simonsen, S. B., Sjolte, J., Steffensen, J. P., Sperlich,
789 P., Sveinbjörnsdóttir, A. E., Vinther, B. M. and White, J. W. C.: Continuous monitoring of summer
790 surface water vapor isotopic composition above the Greenland Ice Sheet, *Atmos. Chem. Phys.*,
791 13(9), 4815–4828, doi:10.5194/acp-13-4815-2013, 2013.
- 792 Steen-Larsen, H. C., Sveinbjörnsdóttir, A. E., Jonsson, T., Ritter, F., Bonne, J.-L., Masson-
793 Delmotte, V., Sodemann, H., Blunier, T., Dahl-Jensen, D. and Vinther, B. M.: Moisture sources

794 and synoptic to seasonal variability of North Atlantic water vapor isotopic composition, *J.*
795 *Geophys. Res. Atmos.*, 120(12), 2015JD023234, doi:10.1002/2015JD023234, 2015.

796 Steen-Larsen, H. C., Sveinbjörnsdóttir, A. E., Peters, A. J., Masson-Delmotte, V., Guishard, M.
797 P., Hsiao, G., Jouzel, J., Noone, D., Warren, J. K. and White, J. W. C.: Climatic controls on water
798 vapor deuterium excess in the marine boundary layer of the North Atlantic based on 500 days of
799 in situ, continuous measurements, *Atmos. Chem. Phys.*, 14(15), 7741–7756, doi:10.5194/acp-14-
800 7741-2014, 2014.

801 Tian, L., Masson-Delmotte, V., Stievenard, M., Yao, T. and Jouzel, J.: Tibetan Plateau summer
802 monsoon northward extent revealed by measurements of water stable isotopes, *J. Geophys. Res.*
803 *Atmos.*, 106(D22), 28081–28088, doi:10.1029/2001JD900186, 2001.

804 Uemura, R., Matsui, Y., Yoshimura, K., Motoyama, H. and Yoshida, N.: Evidence of deuterium
805 excess in water vapor as an indicator of ocean surface conditions, *J. Geophys. Res. Atmos.*,
806 113(D19), n/a–n/a, doi:10.1029/2008JD010209, 2008.

807 Vallet-Coulomb, C., Gasse, F. and Sonzogni, C.: Seasonal evolution of the isotopic composition
808 of atmospheric water vapour above a tropical lake: Deuterium excess and implication for water
809 recycling, *Geochim. Cosmochim. Acta*, 72(19), 4661–4674, doi:10.1016/j.gca.2008.06.025, 2008.

810 Wang, L., Niu, S., Good, S. P., Soderberg, K., McCabe, M. F., Sherry, R. A., Luo, Y., Zhou, X.,
811 Xia, J. and Caylor, K. K.: The effect of warming on grassland evapotranspiration partitioning using
812 laser-based isotope monitoring techniques, *Geochim. Cosmochim. Acta*, 111, 28–38,
813 doi:10.1016/j.gca.2012.12.047, 2013a.

814 Wang, L., Niu, S., Good, S. P., Soderberg, K., McCabe, M. F., Sherry, R. A., Luo, Y., Zhou, X.,
815 Xia, J. and Caylor, K. K.: The effect of warming on grassland evapotranspiration partitioning using
816 laser-based isotope monitoring techniques, *Geochim. Cosmochim. Acta*, 111, 28–38,
817 doi:http://dx.doi.org/10.1016/j.gca.2012.12.047, 2013b.

818 Wei, J., Dirmeyer, P. A., Wisser, D., Bosilovich, M. G. and Mocko, D. M.: Where Does the
819 Irrigation Water Go? An Estimate of the Contribution of Irrigation to Precipitation Using MERRA,
820 *J. Hydrometeorol.*, 14(1), 275–289, doi:10.1175/JHM-D-12-079.1, 2012.

821 Welp, L. R., Lee, X., Griffis, T. J., Wen, X.-F., Xiao, W., Li, S., Sun, X., Hu, Z., Val Martin, M.
822 and Huang, J.: A meta-analysis of water vapor deuterium-excess in the midlatitude atmospheric
823 surface layer, *Global Biogeochem. Cycles*, 26(3), GB3021, doi:10.1029/2011GB004246, 2012.

824 Williams, A. G., Chambers, S. and Griffiths, A.: Bulk Mixing and Decoupling of the Nocturnal
825 Stable Boundary Layer Characterized Using a Ubiquitous Natural Tracer, *Boundary-Layer*
826 *Meteorol.*, 149(3), 381–402, doi:10.1007/s10546-013-9849-3, 2013.

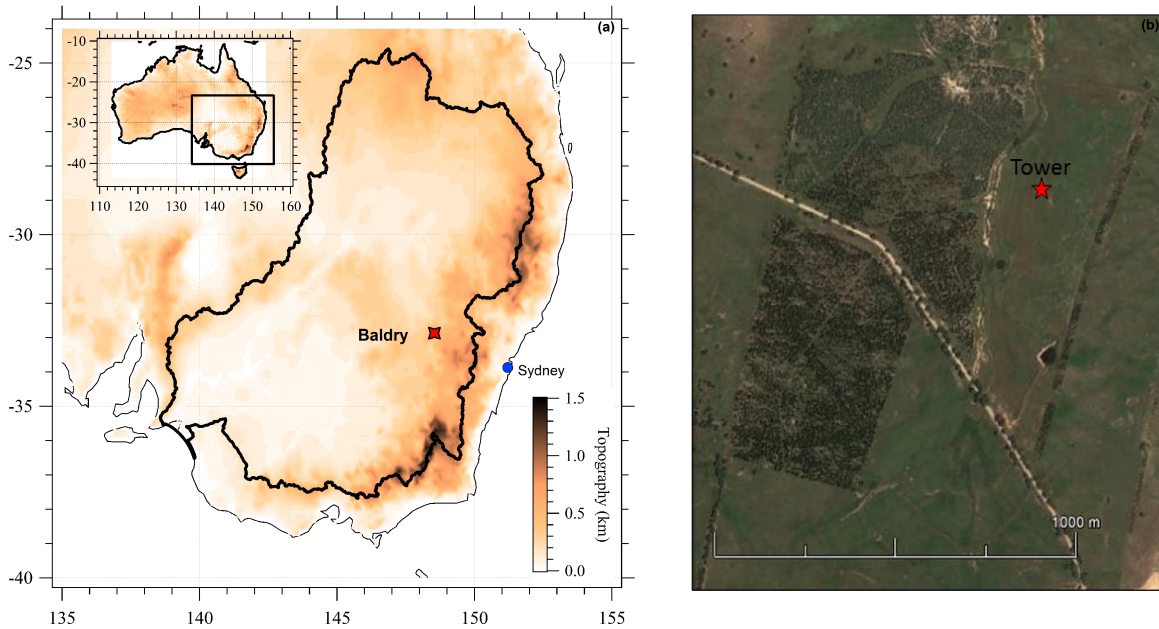
827 Williams, A. G., Zahorowski, W., Chambers, S., Griffiths, A., Hacker, J. M., Element, A. and
828 Werczynski, S.: The Vertical Distribution of Radon in Clear and Cloudy Daytime Terrestrial
829 Boundary Layers, *J. Atmos. Sci.*, 68(1), 155–174, doi:10.1175/2010JAS3576.1, 2010.

830 Xu, X., Werner, M., Butzin, M. and Lohmann, G.: Water isotope variations in the global ocean
831 model MPI-OM, *Geosci. Model Dev.*, 5(3), 809–818, doi:10.5194/gmd-5-809-2012, 2012.

832 Zahorowski, W., Chambers, S. D. and Henderson-Sellers, A.: Ground based radon-222
833 observations and their application to atmospheric studies, *J. Environ. Radioact.*, 76(1–2), 3–33,
834 doi:http://dx.doi.org/10.1016/j.jenvrad.2004.03.033, 2004.

835 Zhao, L., Wang, L., Liu, X., Xiao, H., Ruan, Y. and Zhou, M.: The patterns and implications of
836 diurnal variations in the d-excess of plant water, shallow soil water and air moisture, *Hydrol. Earth*
837 *Syst. Sci.*, 18(10), 4129–4151, doi:10.5194/hess-18-4129-2014, 2014.

838 **8 Figure Captions**

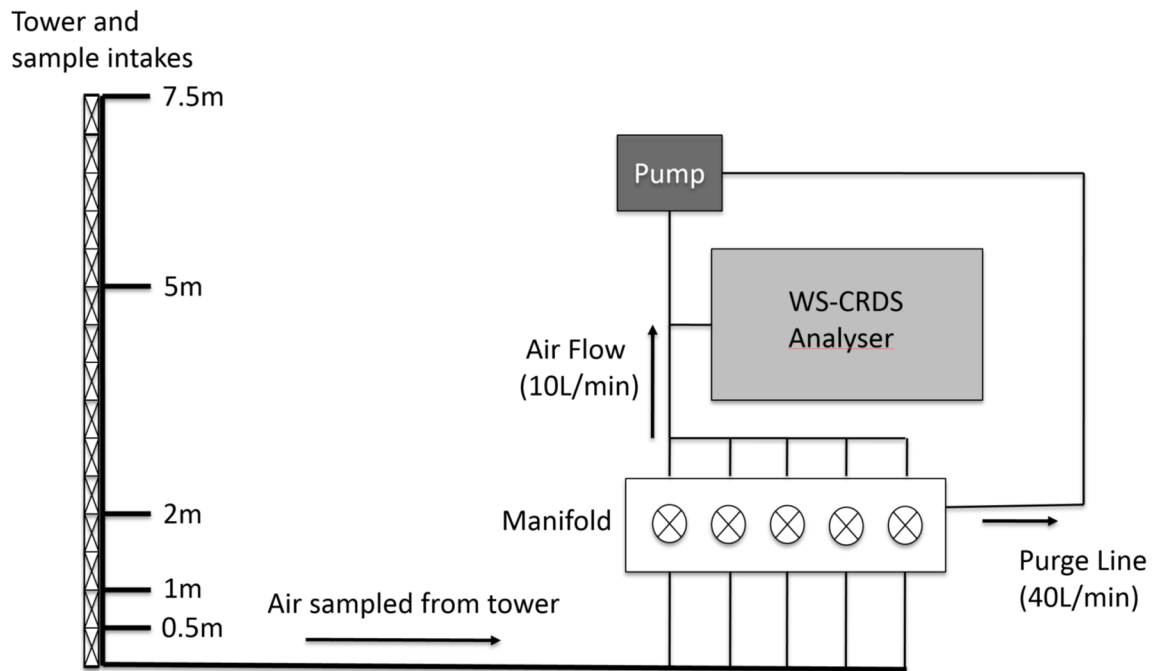


839

Figure 1: a) Location of the Baldry Hydrological Observatory, with the heavy black border outlining the extent of the Murray-Darling Basin, (b) location of the field site used for the campaign, illustrating the semi-arid grassland and adjacent reforested site.

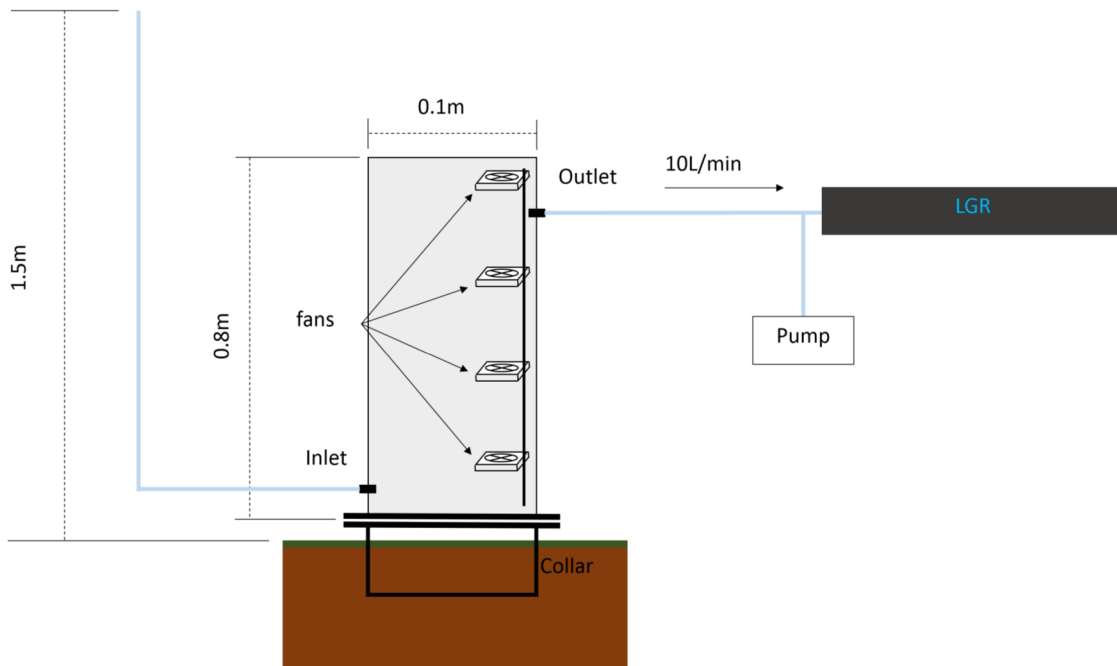
840

841



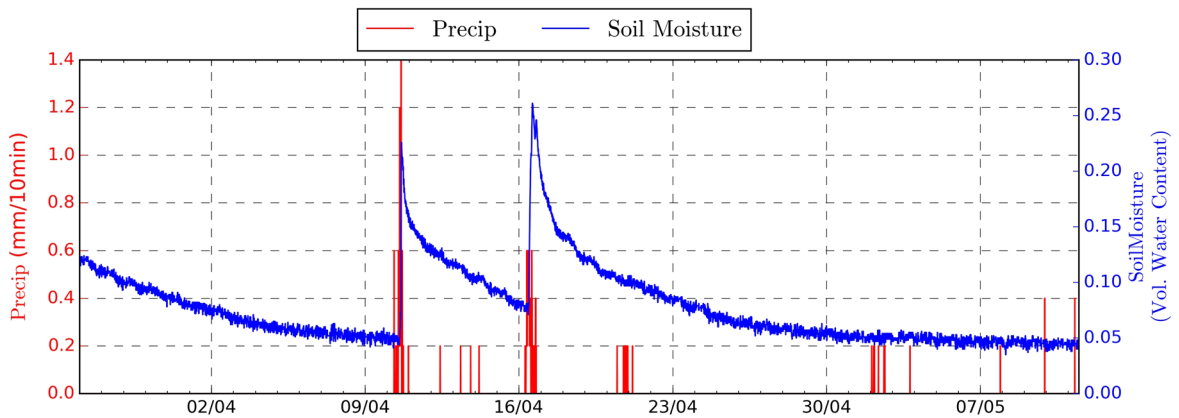
842

843 Figure 2: Sampling system for the automated in-situ collection and measurement of water vapour
844 isotopes from the tower.



845

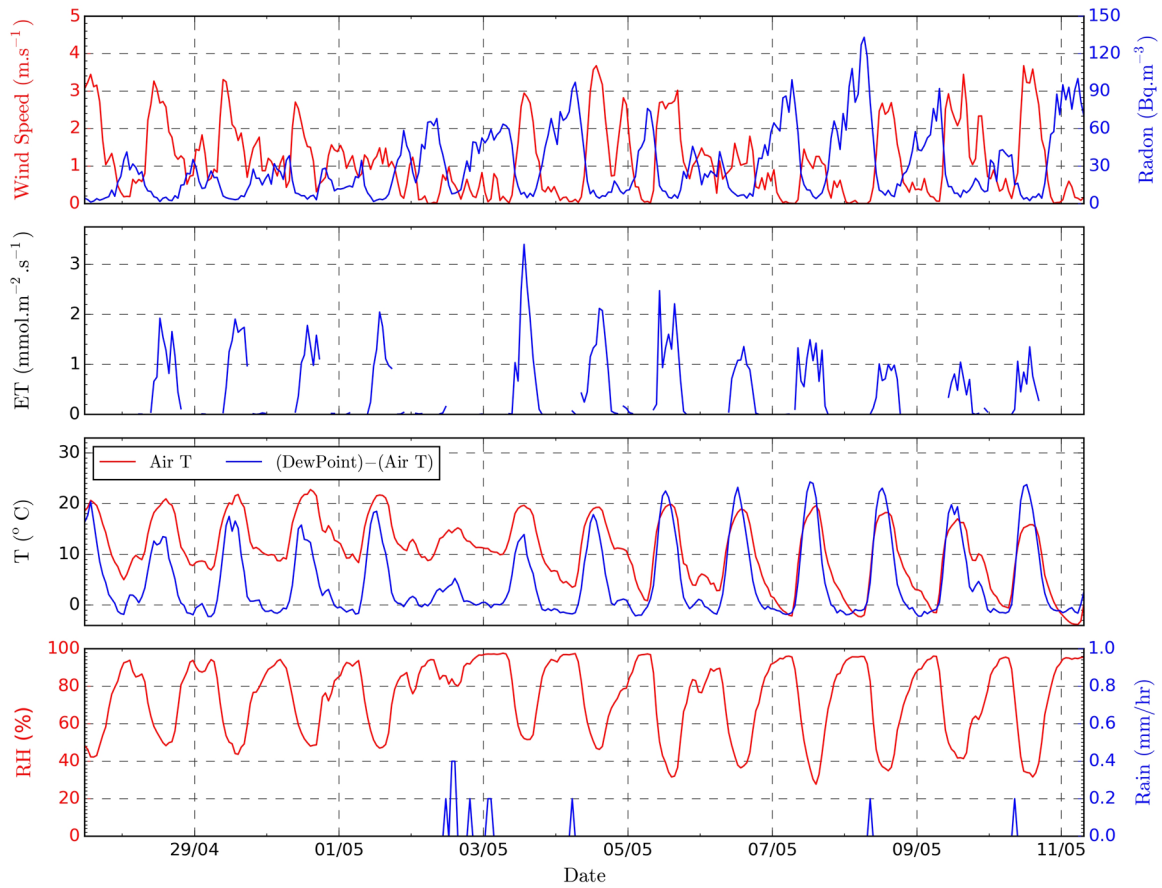
846 Figure 3: Chamber design used for determining the isotopic compositions of ET fluxes.



847

848 Figure 4: Precipitation and 0-10 cm soil moisture for the month leading up to and including the
849 field campaign.

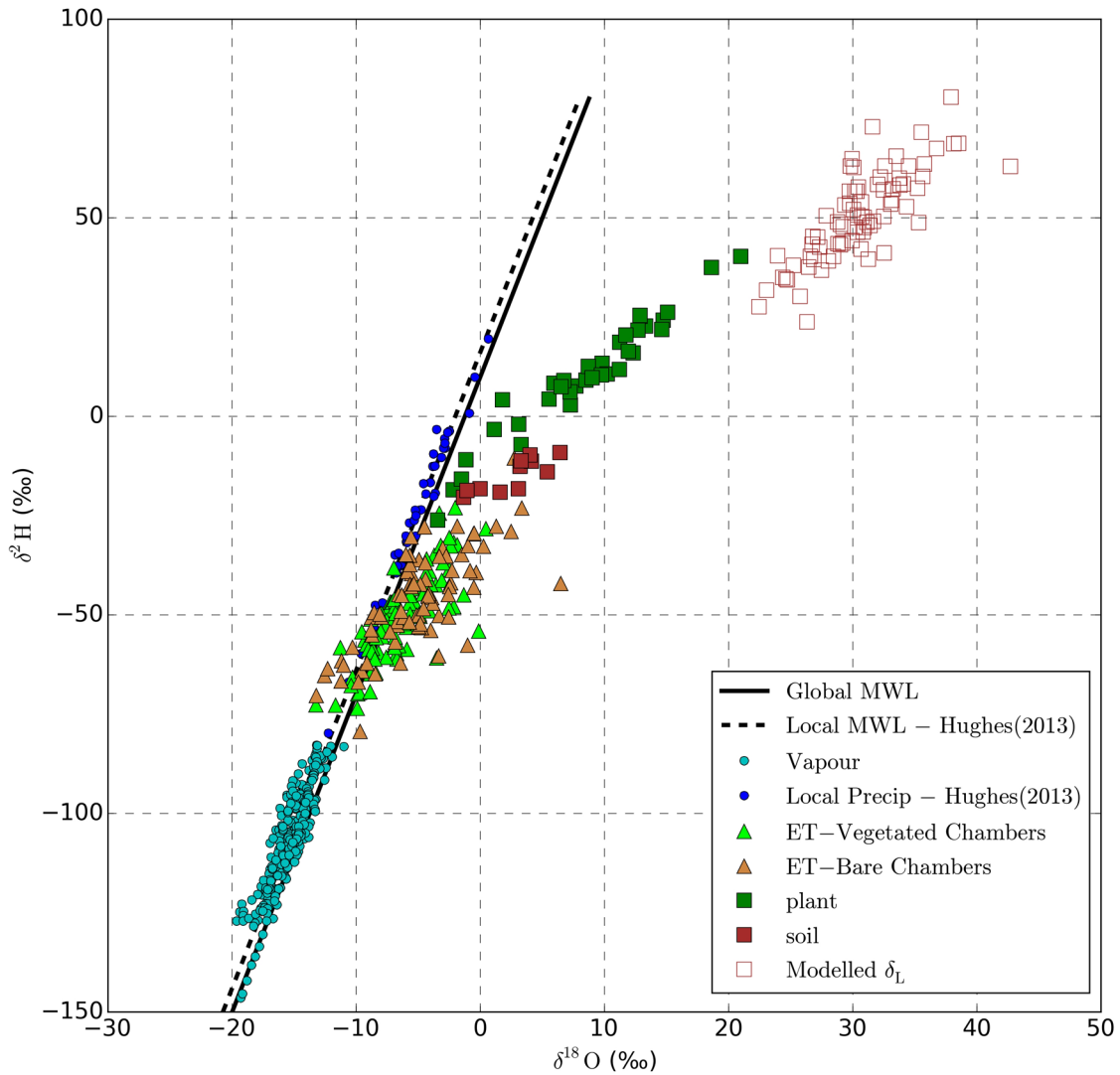
850



851

Figure 5: Meteorological and radon measurements collected throughout the field campaign. Meteorological measurements are block hourly averages calculated from 15-minute observations. Small rain events on the 4th, 8th and 10th May were most likely dew fall rather than precipitation.

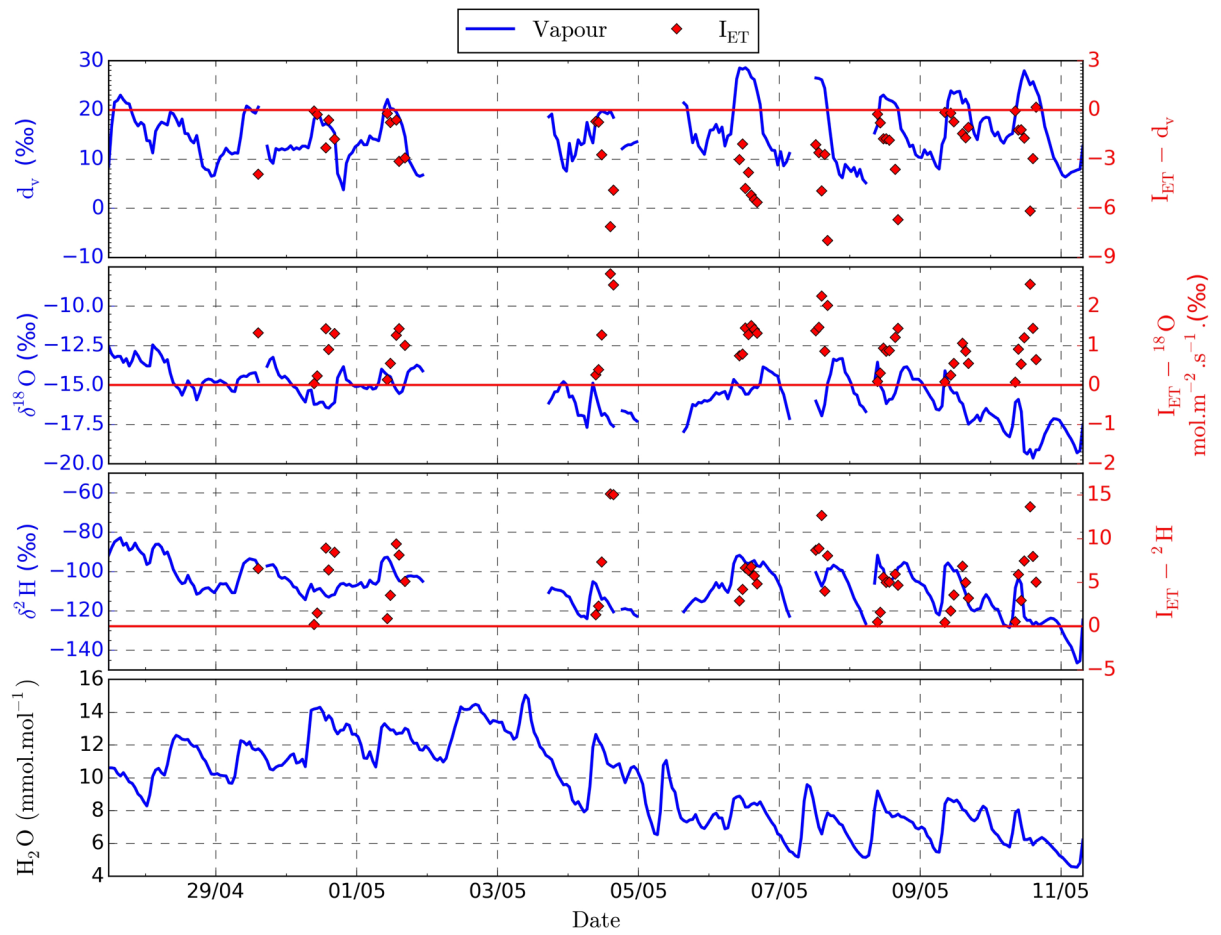
852



853

Figure 6: Relationship between ^2H and ^{18}O for observed and modelled water pools. Linear regressions are shown for local and global meteoric water lines (MWL). Data from Hughes and Crawford (2013) are for monthly cumulative rainfall samples between 2005 and 2008.

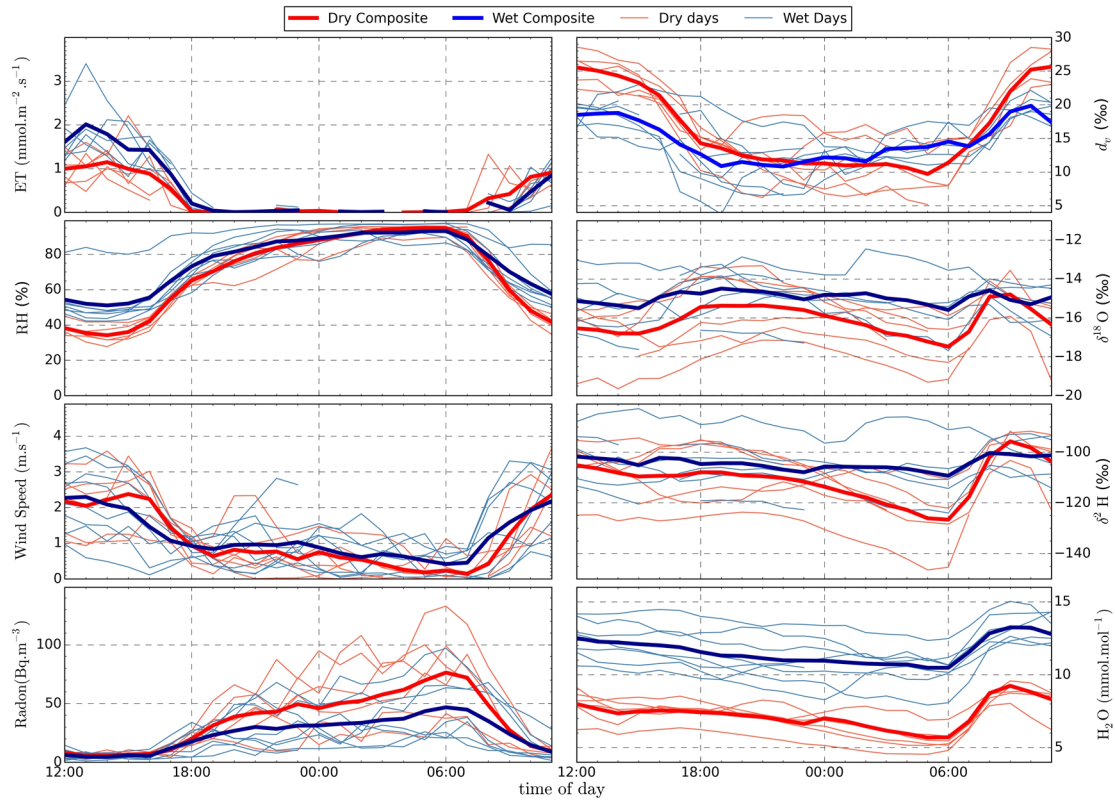
854



855

Figure 7: Time series of hourly water vapour mixing ratio, isotopic composition and ET iso-forcing (I_{ET}).

856



857

Figure 8: Data plotted by time of day and divided into dry and wet periods (see text in section 3.5). Diurnal composites are shown for dry (red) and wet (blue) periods.

858

859 Table 1: Correlation between meteorological variables and the isotopic composition of water
 860 vapour. Values outside the brackets are statistics for the hourly observations. Inside the brackets
 861 are correlation statistics for average values calculated between 11:00 and 15:00 LST, hence
 862 representing activity during a convective boundary layer. Significant correlation are shown in bold;
 863 $p < 0.001$ for hourly observations and $p < 0.05$ for the daytime averages (due to the smaller number
 864 of points).

		T	RH	ET	H₂O	I_{ET}^a
²H	Slope	0.83 (0.51)	-0.17 (0.23)	1.4 (6.1)	2.1 (0.85)	-1.1 (-3.0)
	Intercept	-120 (-140)	-95 (-110)	-110 (-110)	-110 (-130)	-99 (-83)
	R²	0.24 (0.13)	0.09 (0.02)	0.001 (0.04)	0.2 (0.04)	0.2 (0.45)
	p	<0.001 (0.3)	<0.001 (0.7)	0.32 (0.6)	<0.001 (0.5)	0.002 (0.05)
¹⁸O	Slope	0.046 (0.44)	-0.01 (-0.01)	-0.37 (1.8)	0.27 (0.29)	-0.7 (-1.9)
	Intercept	-16 (-24)	-16 (-20)	-15 (-18)	-18 (-19)	-15 (-14)
	R²	0.04 (0.30)	0.004 (0.2)	0.02 (0.16)	0.2 (0.2)	0.14 (0.32)
	p	<0.001 (0.08)	0.26 (0.19)	0.05 (0.26)	<0.001 (0.15)	0.008 (0.11)
<i>d_v</i>	Slope	0.51 (-1.4)	-0.21 (-0.52)	0.01 (-0.16)	0.15 (-1.3)	-1.4 (-2.4)
	Intercept	-9.9 (48)	31 (44)	-15 (-18)	14 (35)	21 (20)
	R²	0.40 (0.48)	0.62 (0.74)	0.22 (0.30)	0.004 (0.71)	0.06 (0.08)
	p	<0.001 (0.02)	<0.001 (<0.01)	0.05 (0.01)	0.26 (<0.01)	0.01 (0.44)

865 ^aIso-forcing correlations were calculated for simultaneous vapour and chamber measurements.
 866 Hourly averaged values were used for both.

867